Bulletin of the Seismological Society of America, Vol. 105, No. 1, pp. 272–284, February 2015, doi: 10.1785/0120140198

Region-Specific Spatial Cross-Correlation Model for Stochastic Simulation of Regionalized Ground-Motion Time Histories

by Duruo Huang and Gang Wang

Abstract Stochastic simulation of spatially distributed ground-motion time histories is important for performance-based earthquake design of geographically distributed systems. In this study, we develop a novel technique to stochastically simulate regionalized ground-motion time histories by taking account of the influence of regional site conditions. For this purpose, a transient acceleration time history is characterized by wavelet-packet parameters proposed by Yamamoto and Baker (2013). The wavelet-packet parameters can fully characterize ground-motion time histories in terms of energy content, time–frequency-domain characteristics and time–frequency nonstationarity. This study further investigates the spatial cross correlations of wavelet-packet parameters based on geostatistical analysis of 1500 regionalized ground-motion data from eight well-recorded earthquakes in California, Mexico, Japan, and Taiwan. The linear model of coregionalization (LMC) is used to develop a permissible spatial cross-correlation model for each parameter group. The geostatistical analysis of ground-motion data from different regions reveals significant dependence of the LMC structure on regional site conditions, which can be characterized by the correlation range of V_{S30} in each region. In general, the spatial correlation and cross correlation of wavelet-packet parameters are stronger if the site condition is more homogeneous. The proposed region-specific correlation model improves stochastic simulation of spatially correlated ground motions, as is demonstrated in illustrative examples in this article. The developed method has great potential to be used in computationally based seismic analysis and loss estimation in a regional scale.

Introduction

Modeling spatial variability of earthquake ground motions is essential for evaluating the seismic performance of geographically distributed systems. Lessons learned from recent major earthquakes show that the infrastructure damages are closely related to the spatial distribution of ground-motion intensity measures (IMs). For example, Jeon and O'Rourke (2005) reported the damage pattern of water supply system in Los Angeles, California, is significantly correlated with the spatial distribution of peak ground velocity in the 1994 Northridge earthquake. On the other hand, the extent of damage of existing residential buildings is related to spectrum intensity (O'Rourke and Jeon, 2002; Jeon and O'Rourke, 2005). The spatial variability of ground-motion IMs has been found to be important in regional seismic-hazard analysis and loss estimation (e.g., Sokolov and Wenzel, 2011; Du and Wang, 2014).

Over the past years, models have been developed to estimate spatial correlations of various scalar ground-motion IMs (e.g., Goda and Hong, 2008; Jayaram and Baker, 2009; Esposito and Iervolino, 2011; Du and Wang, 2013b), as well as a spatial cross-correlation model to consider the joint spatial relationship between vector IMs (Loth and Baker, 2013; Wang and Du, 2013). Observations from strong-motion data in California, Japan, and Taiwan also indicate the spatial correlation of IMs attenuates over separation distance quite differently in different regions. Spatial correlation appears to be greater if the correlation range of average shear-wave velocity in the upper 30 m (V_{S30}) is larger (Jayaram and Baker, 2009; Sokolov *et al.*, 2012; Du and Wang, 2013b; Sokolov and Wenzel, 2013). To quantify the influence of site conditions on the spatial cross correlations of vector IMs, Wang and Du (2013) proposed a linear model of coregionalization to account for the correlation range of V_{S30}.

However, knowing ground-motion IMs is not sufficient to construct specific ground-motion waveforms, which is needed in performance-based design and nonlinear structural analysis. Most recently, Huang and Wang (2014) proposed a stochastic method for direct simulation of regionalized ground-motion time histories. Compared with previous IM studies, the model has two distinctive features: (1) a transient ground-motion time history is characterized using the wavelet packet following Yamamoto and Baker (2013). The wavelet-packet transform is a time–frequency analysis tool

Table 1
Earthquake Events Used in This Study

Event	Date (yyyy/mm/dd)	Moment Magnitude	Location	Number of Recordings	Correlation Range $R_{V_{S30}}$ (km)
Northridge	1994/01/17	6.7	California	152	0
Chi-Chi	1999/09/20	7.6	Taiwan	381	36
Parkfield	2004/09/28	6.0	California	90	4
Anza	2005/06/12	5.2	California	111	24
Chuetsu	2007/07/16	6.8	Japan	114	20
Alum Rock	2007/10/30	5.4	California	161	17
Chino Hills	2008/07/29	5.4	California	337	31
El Mayor Cucapah	2010/04/04	7.2	Mexico	154	23

that decomposes a ground-motion time series into a set of wavelet packets localized in the time and frequency domain. Using the inverse transformation, waveforms can be reconstructed. Thirteen wavelet parameters can fully characterize the energy, time domain, frequency content, and nonstationary features of ground motions. Meanwhile, they can be used to construct ground-motion waveforms according to seismological variables such as earthquake magnitude, source-to-site distance, and site conditions (Yamamoto and Baker, 2013). (2) Spatial cross correlations of these wavelet-packet parameters are determined through geostatistical analysis of well-populated earthquake data. Using the spatial cross-correlation model, spatially distributed ground-motion time histories can be constructed given a scenario earthquake. Furthermore, given recorded time histories at nearby sites, wavelet parameters can be statistically estimated at any unmeasured location. Accordingly, regionalized ground-motion waveforms can be constructed over the study region using the spatially correlated wavelet-packet parameters (Huang and Wang, 2014). The method is one step further toward computationally based seismic analysis and loss estimation in a regional scale.

Similar to previous IM studies, geostatistical analysis also reveals significant difference in the spatial correlations of wavelet parameters, using ground-motion data from the 1994 Northridge and the 1999 Chi-Chi earthquakes (Huang and Wang, 2014). The observation calls for the development of a region-specific spatial correlation model to account for the influence of regional site conditions. One of the major challenges in developing such a model is the availability of densely populated ground-motion data in different regions. In this study, we compiled 1500 regionalized strong-motion records from eight recent earthquakes occurred in California, Mexico, Japan, and Taiwan, with updated geological information in each region. The abundance of ground-motion data facilitates the analysis of spatial cross correlations of wavelet parameters and their dependency on regional geological conditions. In this study, we will develop a permissible spatial cross-correlation model of wavelet parameters by taking into account the influence of regional site conditions described by the correlation range of V_{S30}. An illustrative example is provided to highlight the influence of regional site conditions in the simulation of regionalized ground-motion time histories.

Regionalized Strong-Motion Data and Regional Site Conditions

Regionalized Strong-Motion Data

A total of 1500 regionalized ground-motion records from eight recent earthquakes in California, Mexico, Japan, and Taiwan are adopted in this study. Table 1 provides detailed information of these events. They are the 1994 Northridge earthquake, 1999 Chi-Chi earthquake, 2004 Parkfield earthquake, 2005 Anza earthquake, 2007 Alum Rock earthquake, 2007 Chuetsu earthquake, 2008 Chino Hills earthquake, and 2010 El Mayor Cucapah earthquake. Ground-motion time histories of these events were retrieved from the Center for Engineering Strong-Motion Data, Consortium of Organizations for Strong-Motion Observation Systems (COSMOS), for California earthquakes, and from K-NET for Japan earthquakes. All of these ground-motion records were postprocessed following the Pacific Earthquake Engineering Research (PEER) processing methodology to remove long-period drift and high-frequency noises (Ancheta *et al.*, 2013). Seismic information for these events and geological conditions for recording stations are obtained from the PEER Center's Next Generation Attenuation-West 2 Project (NGA-West 2) strong-motion database and the table S1 database provided by Kaklamanos and Baise (2011).

Figure 1 shows the V_{S30} maps and locations of seismograph stations for the eight events considered in this study. The V_{S30} maps (compare with Fig. 1) are estimated based on topographic slope, obtained from the global V_{S30} map server hosted by U.S. Geological Survey (Allen and Wald, 2009). It should be noted that V_{S30} values used to perform geostatistical analyses in the following sections are still obtained from the PEER NGA-West 2 and S1 database, as these values are considered to be more accurate than those from the global V_{S30} map.

Semivariogram Analysis of V_{S30} in Different Regions

To quantify the influence of regional geology conditions, semivariogram analysis is used to characterize the spatial dissimilarity of V_{S30} over the study regions. Semivariogram of a regionalized variable can be estimated as

$$\tilde{\gamma}(h) = \frac{1}{2|N(h)|}\sum_{i=1}^{N(h)}[z(u_\alpha + h) - z(u_\alpha)]^2, \qquad (1)$$

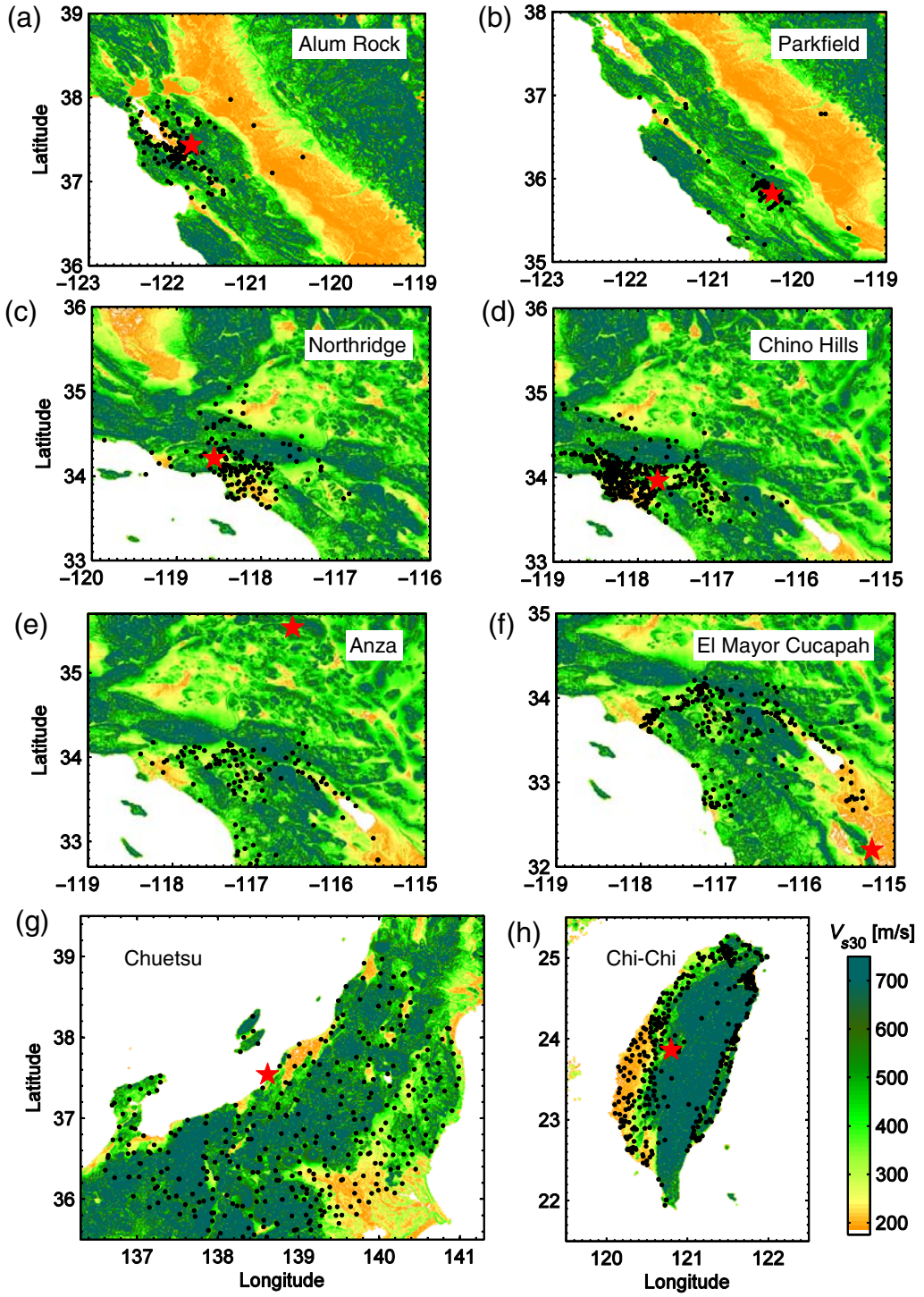

Figure 1. The V_{S30} maps and locations of earthquake recording stations used in this study (stations, dots; epicenters, stars; latitude and longitude are in degrees). The color version of this figure is available only in the electronic edition.

in which $z(u_\alpha)$ denotes V_{S30} value at the recording location u_α, $\tilde{\gamma}(h)$ denotes the estimated semivariogram for two locations separated by distance h, and $N(h)$ is the number of distinct data pairs in the separation distance bin of $[h - \Delta h, h + \Delta h]$. To fit the empirical semivariograms, an exponential model is selected in this study because it has a simple functional form and can provide the best overall fit of the empirical data:

$$\gamma(h) = a[1 - \exp(-3h/R_{V_{S30}})], \tag{2}$$

in which $R_{V_{S30}}$ represents the range of spatial correlation of V_{S30} (unit in kilometers), to be determined to represent the homogeneity of regional site conditions. In general, a larger $R_{V_{S30}}$ value implies a more homogeneous regional site condition, whereas $R_{V_{S30}} = 0$ implies the regional site condition is

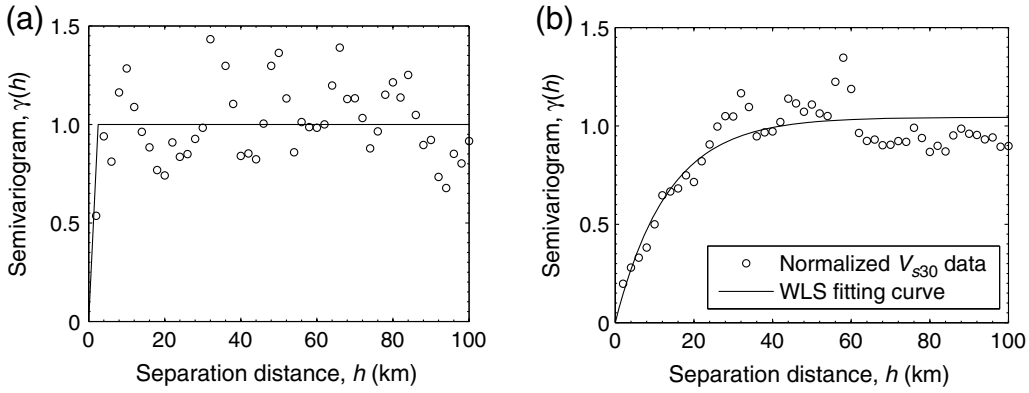

Figure 2. Empirical semivariograms of V_{S30} at the recording stations in (a) the 1994 Northridge earthquake and (b) the 1999 Chi-Chi earthquake.

the most heterogeneous one. As shown in Figure 2a, $R_{V_{S30}} = 0$ can fit the empirical semivariogram data from the 1994 Northridge earthquake, whereas a large correlation range of V_{S30} ($R_{V_{S30}} = 36$ km) is fitted for the 1999 Chi-Chi earthquake as shown in Figure 2b.

It is worth noting that the majority of V_{S30} values in the strong-motion database are not based on direct measurements. Instead, these values were inferred from regional V_{S30} profiles, extrapolated from shallow sites or estimated as a function of site classification and station elevation (Chiou *et al.*, 2008). Previous studies found that the above situation could possibly cause artificially higher estimation of $R_{V_{S30}}$ (Jayaram and Baker, 2009; Baker and Miller, 2011; Du and Wang, 2013b). Accordingly, a correction procedure is implemented in this study to account for the uncertainties in estimating V_{S30} values and to minimize errors in estimating $R_{V_{S30}}$ (Du and Wang, 2013b). The last column of Table 1 provides the estimated $R_{V_{S30}}$ for the eight earthquake events considered in this study, in which $R_{V_{S30}}$ is 0 km for the most heterogeneous case (the Northridge earthquake) and $R_{V_{S30}}$ is up to 36 km for the most homogeneous case (the Chi-Chi earthquake).

Spatial Cross Correlation of Wavelet-Packet Parameters

Wavelet-Packet Parameters for Characterizing Earthquake Ground Motions

This study employs the stochastic model proposed by Yamamoto and Baker (2013) to decompose and reconstruct ground-motion time histories using wavelet packets analysis. The model uses 13 parameters to characterize the distribution of wavelet-packet spectrum in time–frequency domain, along with energy and nonstationary features of a ground-motion time history. Furthermore, wavelets of large amplitude are grouped into a major group, which accounts for 70% of the total waveform energy; whereas the remaining wavelets belong to a minor group. Figure 3 shows an example illustrating the wavelet-packet spectrum of a recorded ground-motion time history at Sun Valley, Roscoe Boulevard station in Los Angeles during the 1994 Northridge earthquake. The wavelet-packet spectrum shows the time and frequency-domain distribution of the squared amplitudes of wavelet-packet coefficients. $E(t)$ and $S(t)$ denote the mean and standard deviation of the spectral distribution in time domain; $E(f)$ and $S(f)$ denote the mean and standard deviation of the spectral distribution in frequency domain. One may refer to Yamamoto and Baker (2013) for detailed definition of each parameter. More recently, Huang and Wang (2014) classified those wavelet parameters into five groups, as presented in Table 2. E_{acc} in group (I) describes the total energy of a ground-motion time history, whereas $E(a)_{major}$ is the averaged spectral coefficient of the major group; parameters in group (II) and (III) describe the statistics (mean E and standard deviation S) of wavelet-packet coefficients in time (t) and frequency (f) domain for the major and minor group, respectively; the time–frequency correlation ρ is used to

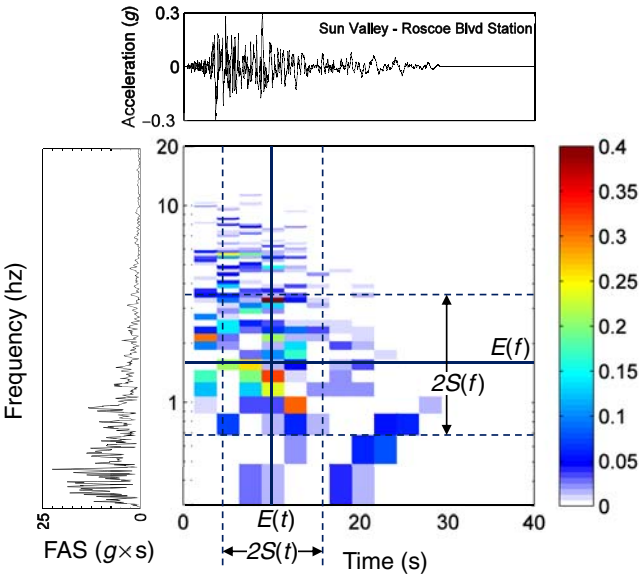

Figure 3. An example of the wavelet-packet spectrum of the recorded waveform at the Sun Valley, Roscoe Boulevard station during the 1994 Northridge earthquake. The color version of this figure is available only in the electronic edition.

Table 2
Summary of Wavelet-Packet Parameters and Parameter Groups

Group (I) Energy Parameters	Group (II) Time-Domain Mean and Standard Deviation	Group (III) Frequency-Domain Mean and Standard Deviation	Group (IV) Time–Frequency Correlation	Randomness Parameter
E_{acc}	$E(t)_{minor}$	$E(f)_{minor}$	$\rho(t,f)_{minor}$	$S(\xi)$
$E(a)_{major}$	$S(t)_{minor}$	$S(f)_{minor}$	$\rho(t,f)_{major}$	
	$E(t)_{major}$	$E(f)_{major}$		
	$S(t)_{major}$	$S(f)_{major}$		

characterize nonstationarity of time series for the major and minor group, as represented by parameters in group (IV). Huang and Wang (2014) found that significant spatial cross correlations exist among parameters in the same group, whereas correlations between groups can be neglected.

Geostatistical Analysis of Intraevent Residuals

Throughout this study, intraevent residuals of wavelet parameters are used to conduct the geostatistical analysis. In general, wavelet parameters can be expressed in the following functional form:

$$Y_{ij} = \overline{Y_{ij}(M,R,V_{S30})} + \eta_i + \varepsilon_{ij}, \tag{3}$$

in which Y_{ij} represents wavelet parameters of an earthquake event i at site j; $\overline{Y_{ij}(M,R,V_{S30})}$ is the predicted mean value of wavelet parameters using the prediction equations proposed by Yamamoto and Baker (2013); η_i and ε_{ij} represent the interevent and intraevent residuals, respectively. It is worth pointing out that the intraevent residuals obtained from equation (3) are corrected to remove bias against the rupture distance for each earthquake event. Furthermore, they are normalized using the sample standard deviation as follows:

$$\varepsilon'_{ij} = \frac{\varepsilon^{corr}_{ij}}{\sigma_{ij}} = \frac{\varepsilon_{ij} - [\varphi_1 + \varphi_2 \ln(R_{rup})]}{\sigma_{ij}}, \tag{4}$$

in which σ_{ij} denotes the sample standard deviation, and φ_1 and φ_2 denote correction coefficients obtained by linear regression for each event. One may refer to Huang and Wang (2014) for a detailed explanation of the procedure.

Compared with previous semivariogram analysis for a single variable, cross semivariogram analysis is often used to estimate the spatial dissimilarity between two variables Z_i and Z_j, (for example, in Jayaram and Baker, 2009, and Wang and Du, 2013). The empirical cross semivariogram $\tilde{\gamma}_{ij}(h)$ can be estimated as (Goovaerts, 1997)

$$\tilde{\gamma}_{ij}(h) = \frac{1}{2|N(h)|}\sum_{\alpha=1}^{N(h)}\left\{\left[z_i(u_\alpha + h) - z_i(u_\alpha)\right] \times \left[z_j(u_\alpha + h) - z_j(u_\alpha)\right]\right\}, \tag{5}$$

in which $z_i(u_\alpha)$ denotes the normalized residuals of ith wavelet parameter at location u_α; h denotes the separation distance in the unit of kilometers.

Linear Model of Coregionalization for Wavelet-Packet Parameters

In this study, the linear model of coregionalization (LMC) is used to construct a permissible cross-semivariogram model, which combines a set of basic functions $g_l(h)$ to fit the empirical cross semivariograms, such that

$$\tilde{\gamma}_{ij}(h) = \sum_{l=1}^{L} b^l_{ij} g_l(h), \tag{6}$$

in which b^l_{ij} represents the sill, which can also be interpreted as the variance contribution of the corresponding basic function $g_l(h)$ (Goovaerts, 1997). In a matrix notation, the permissible cross-semivariogram matrix can be written as

$$\mathbf{\Gamma}(h) = [\gamma_{ij}(h)] = \sum_{l=1}^{L} \mathbf{B}^l g_l(h) \quad i,j = 1,\ldots,n; \quad l = 1,2,\ldots,L, \tag{7}$$

in which $\mathbf{B}^l = [b^l_{ij}]$ is the $n \times n$ coregionalization matrix if n variables are considered. In this study, two exponential basic functions are combined to fit the empirical cross semivariograms, with one as a short range (5 km) function and the other as a long range (60 km) function. The correlation ranges 5 km and 60 km are selected because this LMC structure effectively captures key characteristics of empirical cross semivariograms and provides the best overall fit of the data from the eight earthquakes adopted in this study. Finally, the cross-semivariogram matrix $\mathbf{\Gamma}(h)$ is written in the following form:

$$\mathbf{\Gamma}(h) = \mathbf{B}^1\left[1 - \exp\left(\frac{-3h}{5}\right)\right] + \mathbf{B}^2\left[1 - \exp\left(\frac{-3h}{60}\right)\right]. \tag{8}$$

Accordingly, the covariance matrix $\mathbf{C}(h)$ can be written in the following form:

$$\mathbf{C}(h) = \mathbf{B}^1 \exp\left(\frac{-3h}{5}\right) + \mathbf{B}^2 \exp\left(\frac{-3h}{60}\right). \tag{9}$$

Moreover, the elements b^l_{ij} in the coregionalization matrix $\mathbf{B}^l$ can be standardized following:

$$p^l_{ij} = \frac{b^l_{ij}}{(\sqrt{b^1_{ii} + b^2_{ii}}) \times (\sqrt{b^1_{jj} + b^2_{jj}})}. \tag{10}$$

Accordingly, the correlation matrix $\mathbf{R}(h) = [\rho_{ij}(h)]$ can be written as a function of h and $R_{V_{S30}}$,

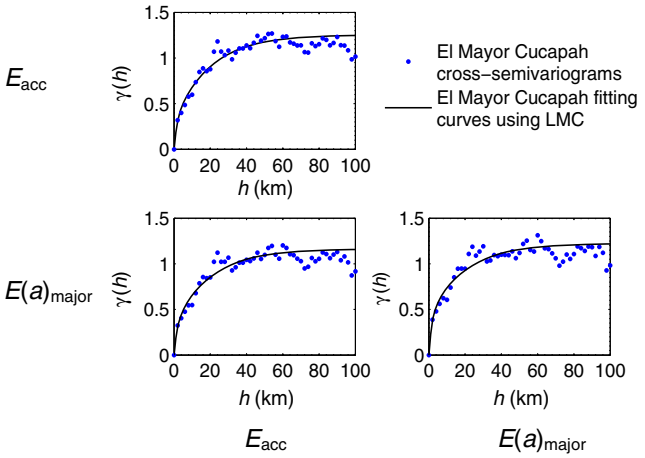

Figure 4. Cross semivariograms of wavelet-packet parameters E_{acc} and $E(a)_{major}$ and fitted linear model of coregionalization curves for the El Mayor Cucapah earthquake. The color version of this figure is available only in the electronic edition.

$$\mathbf{R}(h, R_{V_{S30}}) = \mathbf{P}^1(R_{V_{S30}}) \exp\left(\frac{-3h}{5}\right) + \mathbf{P}^2(R_{V_{S30}}) \exp\left(\frac{-3h}{60}\right), \quad (11)$$

in which $\mathbf{P}^l = [p^l_{ij}]$ $(i, j = 1, \ldots, n)$ represents the (standardized) coregionalization matrix as a function of regional site condition ($R_{V_{S30}}$). In theory, the standardization of the coregionalization matrices is not necessary if normalized residuals are used, and the data is sufficient and not defective. However, the standardization is normally used in practice to compensate for possible deficiency in the empirical data. Mathematically, it is required that $\mathbf{P}^l$ has to be positive semidefinite, to guarantee the correlation matrix $\mathbf{R}$ to be positive semidefinite (Goovaerts, 1997). It should be noted that the LMC structure in equations (8)–(11) is used to fit all the eight earthquake events throughout this study. The influence of regional site conditions on spatial correlations is represented by the dependency of $\mathbf{P}^l$ on $R_{V_{S30}}$, which will be developed in the next section.

Region-Specific Coregionalization Matrices for Wavelet-Packet Parameters

Figure 4 shows an example of LMC fitting of cross semivariograms for wavelet parameters E_{acc} and $E(a)_{major}$ in the energy group (group I in Table 2) using the El Mayor Cucapah event data. Two coregionalization matrices $\mathbf{P}^1$ and $\mathbf{P}^2$ (2×2 in dimension) can be obtained in this case. We also performed similar analysis for all groups of wavelet parameters in Table 2. A similarly good quality of fitting can be observed.

Taking the energy group parameters (group I) as an example, we plotted each element of $\mathbf{P}^1$ and $\mathbf{P}^2$ matrices over $R_{V_{S30}}$ to illustrate its dependency on the regional site conditions, as shown in Figure 5. All the elements in the short-range matrix $\mathbf{P}^1$ show a clear trend that linearly decreases with increasing $R_{V_{S30}}$. On the other hand, the long-range matrix $\mathbf{P}^2$ increases linearly with the increase of $R_{V_{S30}}$. We propose the

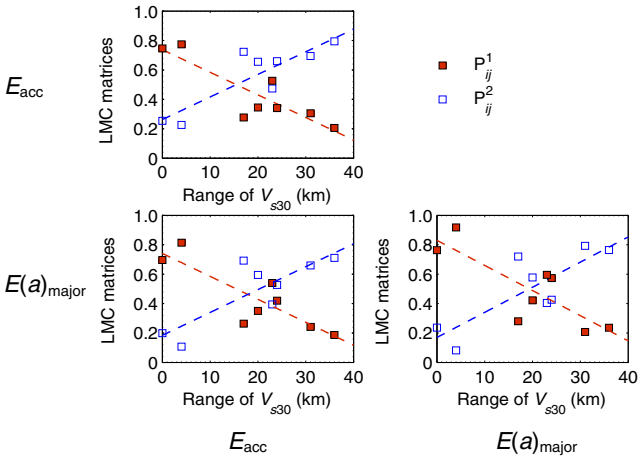

Figure 5. Coregionalization matrices $\mathbf{P}^1_{(I)}$ and $\mathbf{P}^2_{(I)}$ for group (I) parameters E_{acc} and $E(a)_{major}$ over $R_{V_{S30}}$ for the eight events considered in this study (points, empirical data; lines, linear predictive model via equation 12). The color version of this figure is available only in the electronic edition.

following models to describe the linear dependency of $\mathbf{P}^1$ and $\mathbf{P}^2$ on $R_{V_{S30}}$:

$$\mathbf{P}^1_{(*)}(R_{V_{S30}}) = \mathbf{P}^{01}_{(*)} - \mathbf{K}_{(*)}\left(\frac{R_{V_{S30}}}{10}\right)$$

and

$$\mathbf{P}^2_{(*)}(R_{V_{S30}}) = \mathbf{P}^{02}_{(*)} + \mathbf{K}_{(*)}\left(\frac{R_{V_{S30}}}{10}\right), \quad (12)$$

in which the subscript $(*) =$ (I), (II), (III), (IV) are used to indicate different parameter groups, for which the dimensions of matrices are different for different groups; $R_{V_{S30}}$ is the correlation range of V_{S30} (unit in kilometers); $\mathbf{P}^{01}_{(*)}$, $\mathbf{P}^{02}_{(*)}$, and $\mathbf{K}_{(*)}$ are constant matrices to be determined by linear regression analyses for each parameter group.

It is interesting to notice that a similar form of equation (12) has also been used in describing the regional cross-correlation structure of vector IMs in a recent study (Wang and Du, 2013). To guarantee a positive-semidefiniteness of the correlation matrix, all matrices $\mathbf{P}^{01}_{(*)}$, $\mathbf{P}^{02}_{(*)}$, and $\mathbf{K}_{(*)}$ have to be positive-semidefinite. Moreover, on the condition that the separation distance $h = 0$, the local correlation matrix $\mathbf{R}(0) = \mathbf{P}^{01}_{(*)} + \mathbf{P}^{02}_{(*)}$ following equations (11) and (12). Therefore, $\mathbf{P}^{01}_{(*)}$ and $\mathbf{P}^{02}_{(*)}$ can be regarded as partition of the local correlation matrix $\mathbf{R}(0)$. $\mathbf{K}_{(*)}$ represents the rate of dependency on the regional site differences.

Taking parameters E_{acc} and $E(a)_{major}$ in group (I) as an example, $\mathbf{P}^{01}_{(I)}$, $\mathbf{P}^{02}_{(I)}$, and $\mathbf{K}_{(I)}$ matrices are computed as follows:

$$\mathbf{P}^{01}_{(I)} = \begin{bmatrix} 0.74 & 0.74 \\ 0.74 & 0.83 \end{bmatrix}, \quad \mathbf{P}^{02}_{(I)} = \begin{bmatrix} 0.26 & 0.18 \\ 0.18 & 0.17 \end{bmatrix},$$
$$\mathbf{K}_{(I)} = \begin{bmatrix} 0.16 & 0.16 \\ 0.16 & 0.17 \end{bmatrix}. \quad (13)$$

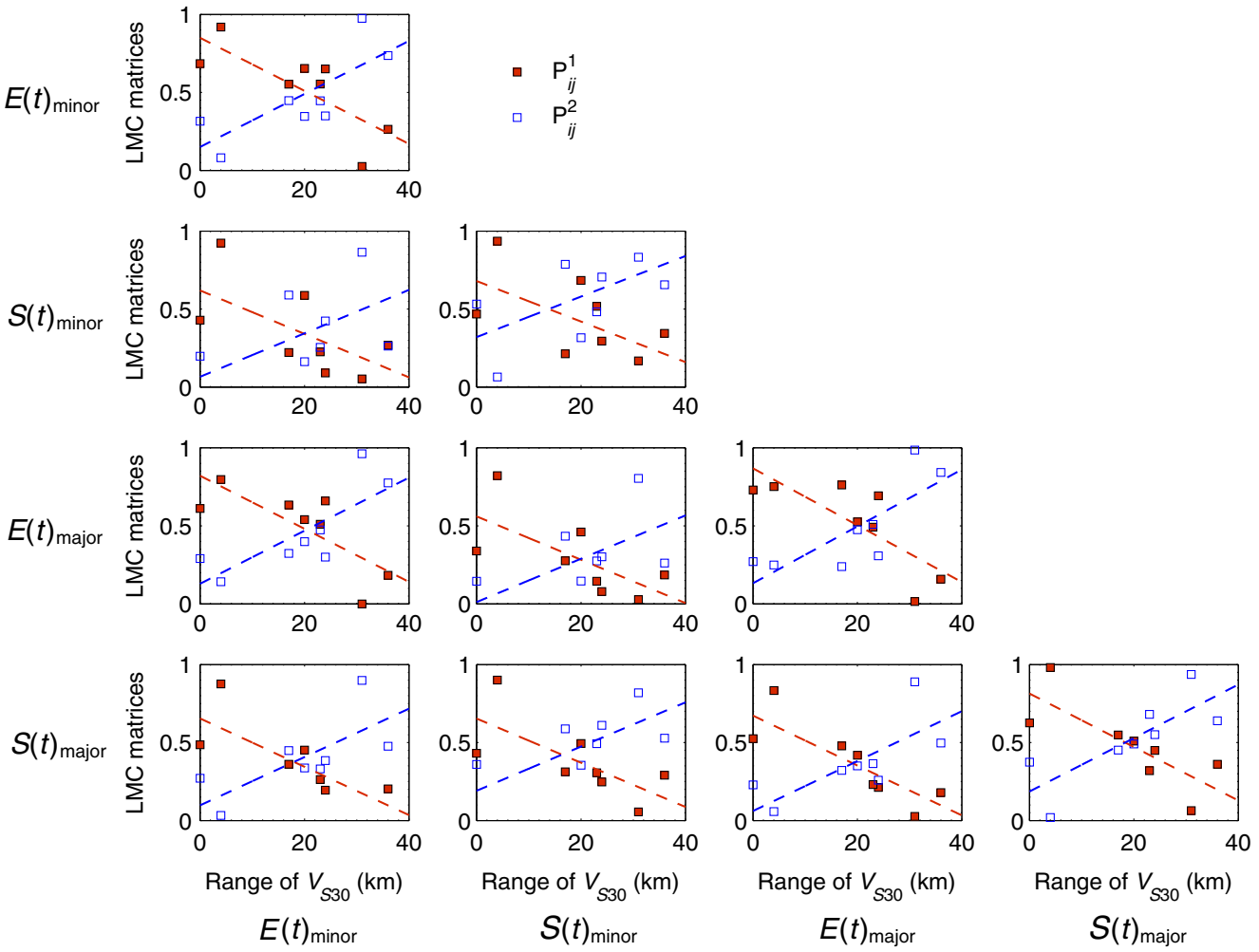

Figure 6. Coregionalization matrices $\mathbf{P}^1_{(\mathrm{II})}$ and $\mathbf{P}^2_{(\mathrm{II})}$ for group (II) time-domain wavelet parameters $E(t)_{\mathrm{minor}}$, $S(t)_{\mathrm{minor}}$, $E(t)_{\mathrm{major}}$, and $S(t)_{\mathrm{major}}$ over $R_{V_{S30}}$ for the eight events in this study. The color version of this figure is available only in the electronic edition.

It is easy to verify that $\mathbf{P}^{01}_{(*)}$, $\mathbf{P}^{02}_{(*)}$, and $\mathbf{K}_{(*)}$ are all positive definite. Obviously, the positive definiteness of $\mathbf{P}^2_{(*)}$ is always guaranteed because it is the summation of two positive-definite matrices. On the other hand, the positive-definiteness of $\mathbf{P}^1_{(*)}$ can only be guaranteed for a limited range of $R_{V_{S30}}$. However, if we can check $\mathbf{P}^1_{(*)}$ is positive definite for $R_{V_{S30}} = \Delta$ km, then the matrix is guaranteed to be positive definite for all cases $R_{V_{S30}} < \Delta$ km. The above mathematical property can be easily proved based on equation (12) as follows:

$$\mathbf{P}^1_{(*)}(\Delta) = \mathbf{P}^{01}_{(*)} - \mathbf{K}_{(*)}\left(\frac{\Delta}{10}\right)$$

and

$$\mathbf{P}^1_{(*)}(R_{V_{S30}} < \Delta) = \mathbf{P}^{01}_{(*)} - \mathbf{K}_{(*)}\left(\frac{R_{V_{S30}}}{10}\right). \quad (14)$$

Therefore,

$$\mathbf{P}^1_{(*)}(R_{V_{S30}} < \Delta) = \mathbf{P}^1_{(*)}(\Delta) + \mathbf{K}_{(*)}\left(\frac{\Delta - R_{V_{S30}}}{10}\right), \quad (15)$$

which is always positive definite as long as $\mathbf{P}^1_{(*)}(\Delta)$ is positive definite. In view of this, we verified that $\mathbf{P}^1_{(*)}$ is positive definite for $R_{V_{S30}} = 40$ km, therefore it is positive definite for all cases of $R_{V_{S30}} \leq 40$ km. In addition, $\mathbf{R}(h=0) = \mathbf{P}^{01}_{(\mathrm{I})} + \mathbf{P}^{02}_{(\mathrm{I})} = \begin{bmatrix} 1 & 0.92 \\ 0.92 & 1 \end{bmatrix}$, indicating a strong local correlation between E_{acc} and $E(a)_{\mathrm{major}}$. The result agrees well with that reported by Yamamoto (2011) using the NGA strong-motion database, which reads

$$\mathbf{R}(h=0) = \begin{bmatrix} \rho_{E_{\mathrm{acc}},E_{\mathrm{acc}}} & \rho_{E_{\mathrm{acc}},E(a)_{\mathrm{major}}} \\ \rho_{E(a)_{\mathrm{major}},E_{\mathrm{acc}}} & \rho_{E(a)_{\mathrm{major}},E(a)_{\mathrm{major}}} \end{bmatrix} = \begin{bmatrix} 1 & 0.89 \\ 0.89 & 1 \end{bmatrix}. \quad (16)$$

As is also shown in Figure 5, the linear model equation (13) can effectively approximate the trend of coregionalization matrices $\mathbf{P}^1_{(*)}$ and $\mathbf{P}^2_{(*)}$ over $R_{V_{S30}}$. To further describe the goodness of fitting, we proposed a standard deviation matrix $\Sigma_{(*)}$, to quantify the standard deviation of residuals for fitting each entry of $\mathbf{P}^1_{(*)}$ and $\mathbf{P}^2_{(*)}$. It is noted

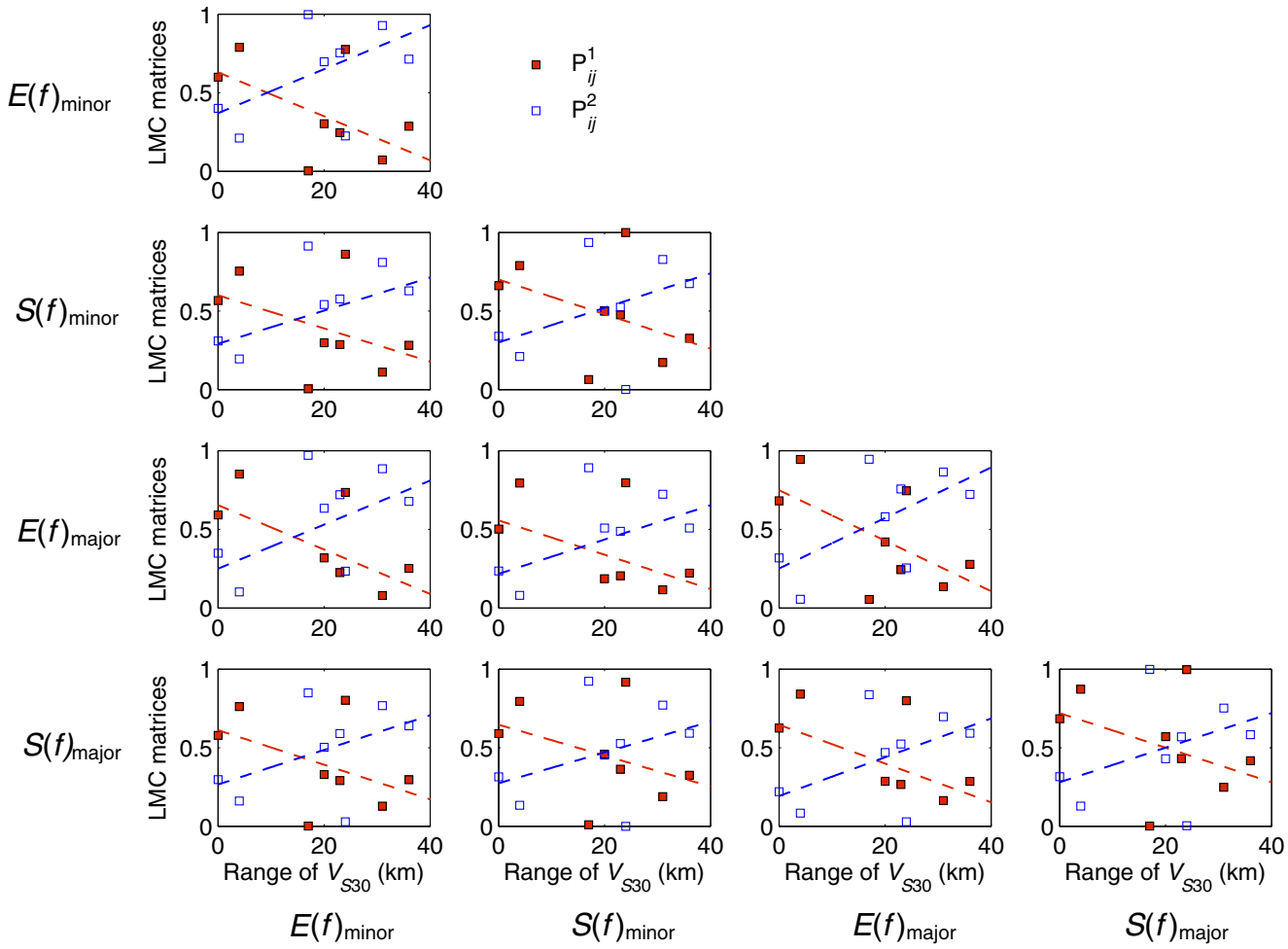

Figure 7. Coregionalization matrices $\mathbf{P}^1_{(\text{III})}$ and $\mathbf{P}^2_{(\text{III})}$ for group (III) frequency-domain wavelet parameters $E(f)_{\text{minor}}$, $S(f)_{\text{minor}}$, $E(f)_{\text{major}}$, and $S(f)_{\text{major}}$ over $R_{V_{S30}}$ for the eight events in this study. The color version of this figure is available only in the electronic edition.

that the standard deviation matrix is the same for both $\mathbf{P}^1_{(*)}$ and $\mathbf{P}^2_{(*)}$. It is computed that $\Sigma_{(\text{I})} = \begin{bmatrix} 0.10 & 0.11 \\ 0.11 & 0.15 \end{bmatrix}$ in the case analyzed above.

Figures 6, 7, 8, and Table 3 summarize the region-specific coregionalization matrices, $\mathbf{P}^{01}_{(*)}$, $\mathbf{P}^{02}_{(*)}$, $\mathbf{K}_{(*)}$, and $\Sigma_{(*)}$, for all four groups of wavelet-packet parameters. First, the linear model equation (12) is used to construct a permissible correlation model for all parameter groups. The resulted correlation matrices via equation (11) all satisfy the mathematical requirement of positive definiteness if $R_{V_{S30}} \leq 40$ km. Second, the dependency of site conditions are ranked in the order of group (I) to group (IV), as indicated by the values of $\mathbf{K}_{(*)}$. The standard deviation of the model fitting generally falls in the range of 0.1–0.3, with the largest errors involved in fitting parameter group (III). Finally, it is worth re-emphasizing that as an overall effect, the spatial correlation for all parameter groups would be stronger if $R_{V_{S30}}$ is larger, that is, the site is more homogeneous. The statement can be easily checked by rewriting the correlation model via equations (11) and (12) as

$$\mathbf{R}(h, R_{V_{S30}}) = \mathbf{P}^{01} \exp\left(\frac{-3h}{5}\right) + \mathbf{P}^{02} \exp\left(\frac{-3h}{60}\right) + \mathbf{K}\left(\frac{R_{V_{S30}}}{10}\right)\left[\exp\left(\frac{-3h}{60}\right) - \exp\left(\frac{-3h}{5}\right)\right]. \quad (17)$$

The conclusion follows as it is obvious that $\exp(\frac{-3h}{60}) - \exp(\frac{-3h}{5})$ in the square bracket is always nonnegative. Finally, it is worth pointing out the correlation model is derived for cases $R_{V_{S30}} \leq 40$ km. The case of $R_{V_{S30}} > 40$ km is less common considering natural variation in geological environment. It is recommended if $R_{V_{S30}} > 40$ km, the results for $R_{V_{S30}} = 40$ km should be used.

Influence of Regional Site Condition on Regionalized Ground-Motion Simulation

Wavelet-packet characterization and spatial correlation of wavelet-packet parameters allow for the development of a new approach to simulate spatially distributed ground motions conditioned on measured neighborhood data. The procedure is recently proposed by Huang and Wang (2014) and is briefly illustrated as follows: First, regionalized

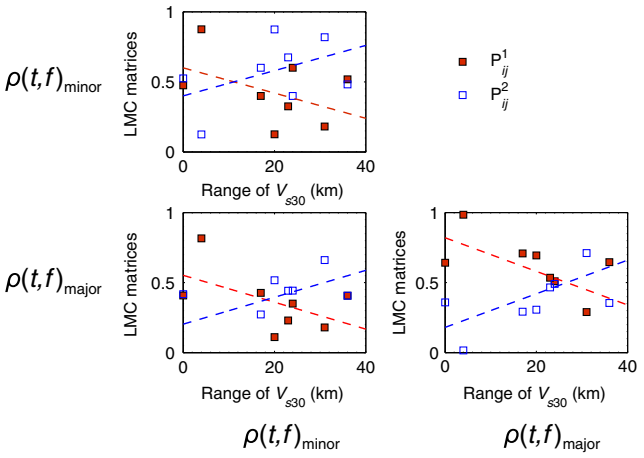

Figure 8. Coregionalization matrices $\mathbf{P}^1_{(IV)}$ and $\mathbf{P}^2_{(IV)}$ for group (IV) nonstationarity wavelet parameters $\rho(t,f)_{major}$ and $\rho(t,f)_{minor}$ over $R_{V_{S30}}$ for the eight events in this study. The color version of this figure is available only in the electronic edition.

ground-motion time histories are decomposed into wavelet-packet parameters; second, wavelet-packet parameters at unmeasured sites are interpolated as weighted summation of parameters at nearby sites, where the weights are determined by the spatial correlation using cokriging analysis; finally, ground-motion time histories at unmeasured sites are constructed using the estimations. In this section, an illustrative example is provided to highlight the importance of regional site conditions in the ground-motion simulation process.

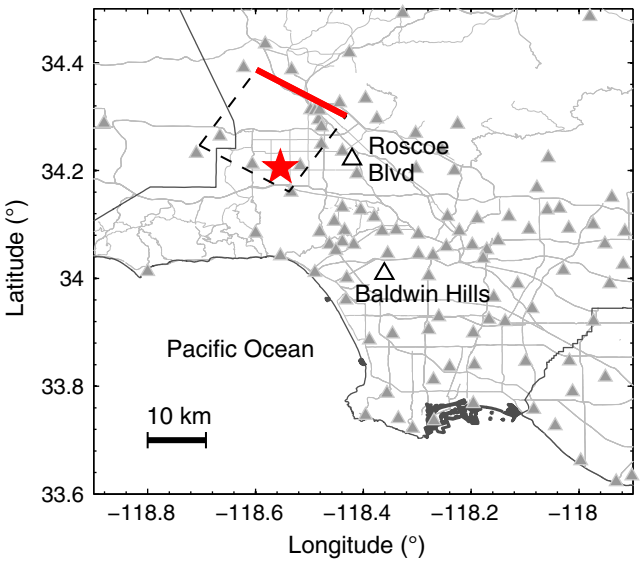

Figure 9. Map of the Los Angeles area showing locations of the two blind-test stations (open triangles). Solid triangles indicate the remaining earthquake recording stations in this region. Epicenter (star), surface fault trace (thick solid line), and projection of subsurface fault (thin dashed line) of the 1994 Northridge earthquake are also plotted. The color version of this figure is available only in the electronic edition.

Figure 9 shows a map of the Los Angeles area, with the epicenter and horizontal projection of the blind-thrust fault of the 1994 Northridge earthquake. Two earthquake recording stations, the Sun Valley, Roscoe Boulevard station and the

Table 3
Region-Specific Coregionalization Matrices for Wavelet-Packet Parameter Groups

Parameter Group*	Region-Specific Coregionalization Matrices
(I)	$\mathbf{P}^{01}_{(I)} = \begin{bmatrix} 0.74 & 0.74 \\ 0.74 & 0.83 \end{bmatrix}$, $\mathbf{P}^{02}_{(I)} = \begin{bmatrix} 0.26 & 0.18 \\ 0.18 & 0.17 \end{bmatrix}$
	$\mathbf{K}_{(I)} = \begin{bmatrix} 0.16 & 0.16 \\ 0.16 & 0.17 \end{bmatrix}$, $\Sigma_{(I)} = \begin{bmatrix} 0.10 & 0.11 \\ 0.11 & 0.15 \end{bmatrix}$
(II)	$\mathbf{P}^{01}_{(II)} = \begin{bmatrix} 0.85 & 0.62 & 0.82 & 0.65 \\ 0.62 & 0.68 & 0.56 & 0.65 \\ 0.82 & 0.56 & 0.87 & 0.67 \\ 0.65 & 0.65 & 0.67 & 0.81 \end{bmatrix}$, $\mathbf{P}^{02}_{(II)} = \begin{bmatrix} 0.15 & 0.07 & 0.13 & 0.10 \\ 0.07 & 0.32 & 0.01 & 0.19 \\ 0.13 & 0.01 & 0.13 & 0.06 \\ 0.10 & 0.19 & 0.06 & 0.19 \end{bmatrix}$
	$\mathbf{K}_{(II)} = \begin{bmatrix} 0.17 & 0.14 & 0.17 & 0.15 \\ 0.14 & 0.13 & 0.14 & 0.14 \\ 0.17 & 0.14 & 0.18 & 0.16 \\ 0.15 & 0.14 & 0.16 & 0.17 \end{bmatrix}$, $\Sigma_{(II)} = \begin{bmatrix} 0.17 & 0.20 & 0.17 & 0.16 \\ 0.20 & 0.21 & 0.18 & 0.17 \\ 0.17 & 0.18 & 0.17 & 0.13 \\ 0.16 & 0.17 & 0.13 & 0.16 \end{bmatrix}$
(III)	$\mathbf{P}^{01}_{(III)} = \begin{bmatrix} 0.63 & 0.60 & 0.65 & 0.61 \\ 0.60 & 0.70 & 0.56 & 0.65 \\ 0.65 & 0.56 & 0.75 & 0.65 \\ 0.61 & 0.65 & 0.65 & 0.72 \end{bmatrix}$, $\mathbf{P}^{02}_{(III)} = \begin{bmatrix} 0.37 & 0.29 & 0.25 & 0.27 \\ 0.29 & 0.30 & 0.22 & 0.27 \\ 0.25 & 0.22 & 0.25 & 0.19 \\ 0.27 & 0.27 & 0.19 & 0.28 \end{bmatrix}$
	$\mathbf{K}_{(III)} = \begin{bmatrix} 0.14 & 0.11 & 0.14 & 0.11 \\ 0.11 & 0.11 & 0.11 & 0.10 \\ 0.14 & 0.11 & 0.16 & 0.12 \\ 0.11 & 0.10 & 0.12 & 0.11 \end{bmatrix}$, $\Sigma_{(III)} = \begin{bmatrix} 0.26 & 0.27 & 0.26 & 0.26 \\ 0.27 & 0.29 & 0.28 & 0.28 \\ 0.26 & 0.28 & 0.25 & 0.27 \\ 0.26 & 0.28 & 0.27 & 0.30 \end{bmatrix}$
(IV)	$\mathbf{P}^{01}_{(IV)} = \begin{bmatrix} 0.60 & 0.55 \\ 0.55 & 0.82 \end{bmatrix}$, $\mathbf{P}^{02}_{(IV)} = \begin{bmatrix} 0.40 & 0.20 \\ 0.20 & 0.18 \end{bmatrix}$
	$\mathbf{K}_{(IV)} = \begin{bmatrix} 0.09 & 0.10 \\ 0.10 & 0.12 \end{bmatrix}$, $\Sigma_{(IV)} = \begin{bmatrix} 0.22 & 0.18 \\ 0.18 & 0.16 \end{bmatrix}$

*Parameters in each group are ordered the same as in Table 2. Zero correlation is assumed between parameters in different groups.

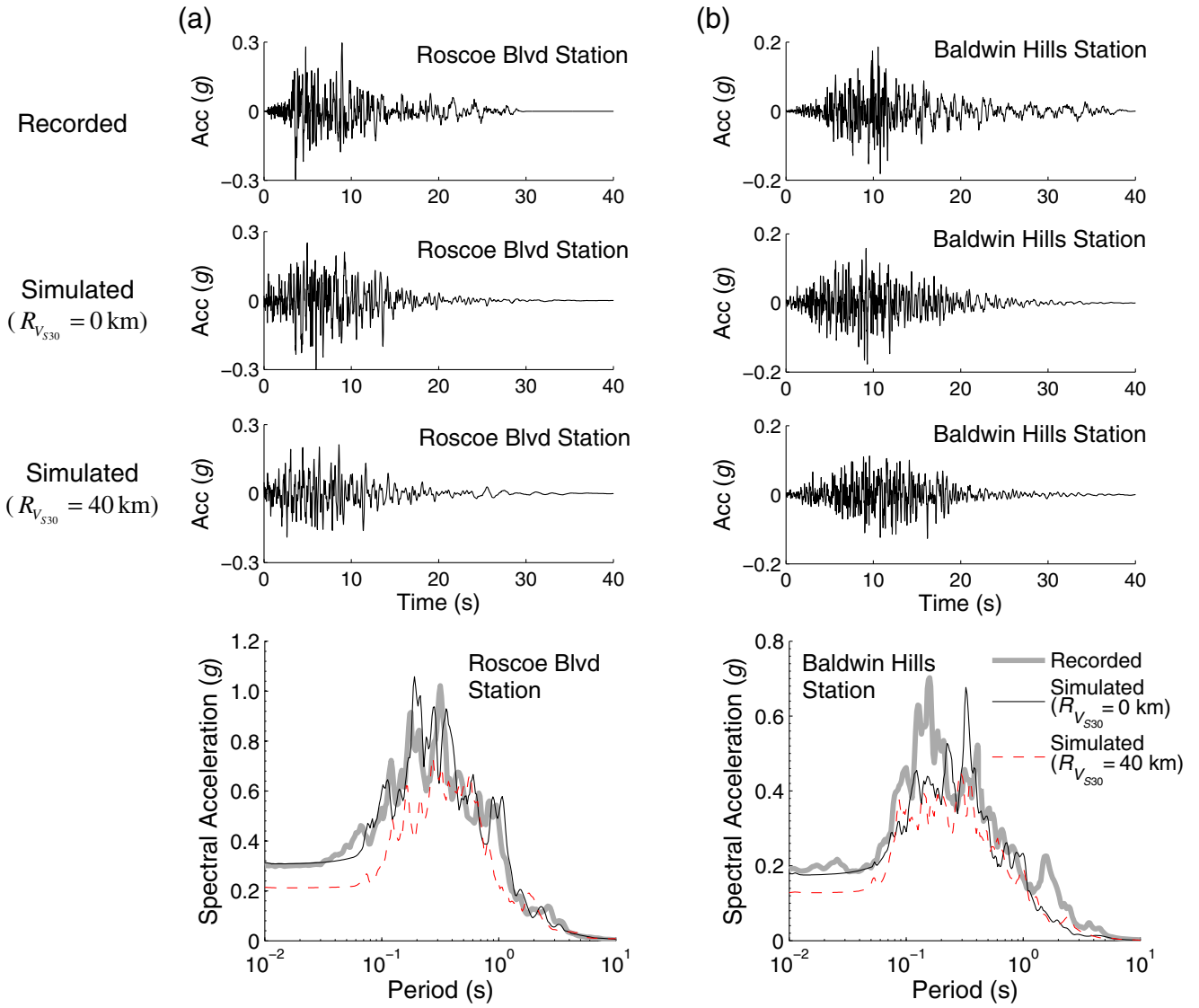

Figure 10. Comparison of recorded and simulated acceleration time histories using different regional site conditions: (a) Sun Valley, Roscoe Boulevard Station (the left column) and (b) Baldwin Hills station (the right column) for the Northridge earthquake. The color version of this figure is available only in the electronic edition.

Baldwin Hills station (marked as open triangles), are selected as the blind-test stations and are treated as unmeasured sites. The real recordings at these two stations are completely removed from the database throughout the blind tests, so that simulated ground motions can be fairly compared with the recorded data.

To demonstrate the influence of regional site conditions on the ground-motion simulation, blind tests are conducted by assuming a heterogeneous regional site condition ($R_{V_{S30}} = 0$ km) and a homogeneous regional site condition ($R_{V_{S30}} = 40$ km). Region-specific coregionalization matrices can be computed using the linear model proposed in equation (15) and in Table 3. Using this spatial cross-correlation model, ordinary cokriging technique is implemented to provide the best linear unbiased estimate of wavelet parameters at the test stations. Accordingly, waveforms at blind-test stations for the Northridge event can be reconstructed using the estimated wavelet parameters. Figure 10 provides comparison between the actually recorded and stochastically simulated ground motions in the blind test.

By visual inspection of the acceleration traces and response spectra in Figure 10, it is observed that the simulated ground motions using the correct correlation model (recall that the actual $R_{V_{S30}} = 0$ km for the Northridge earthquake) agree well with the recorded data at both stations. On the other hand, simulated ground motions assuming a homogeneous regional site condition (i.e., $R_{V_{S30}} = 40$ km) are not consistent with the recorded ones. A similar blind test is also conducted for the Chi-Chi earthquake, as shown in Figure 11 for the earthquake epicenter, the surface projection of the Chelungpu fault, and recording stations in this region. For illustrative purposes, two recording stations are selected to

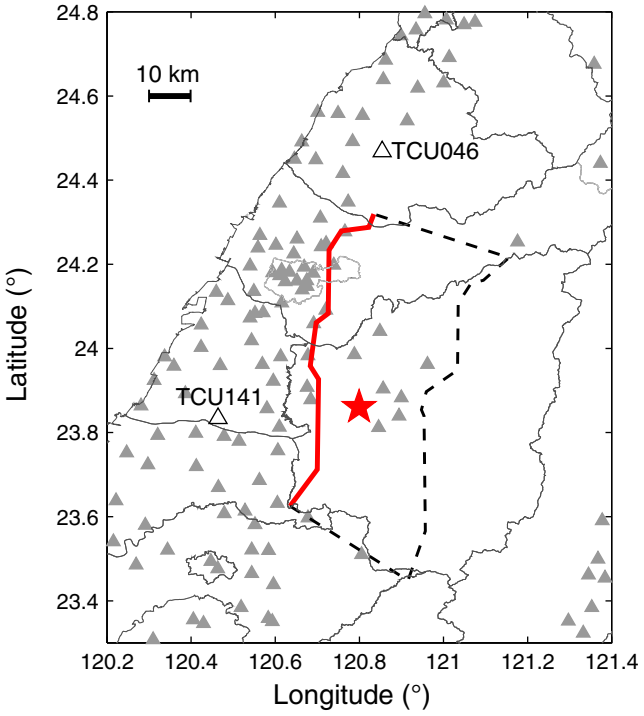

Figure 11. Map of the location of the 1999 Chi-Chi earthquake, showing the two recording stations (TCU046 and TCU141) selected for the blind tests (open triangles). Solid triangles indicate the remaining earthquake recording stations in this region. Epicenter (star), surface fault trace (thick solid line), and projection of subsurface fault (thin dashed line) of the Chi-Chi earthquake are also plotted. The color version of this figure is available only in the electronic edition.

conduct the blind test: TCU046 is in the forward directivity region, where the fault ruptured to the north toward this site; TCU141 is on the footwall side of the fault plane. Rupture distances of the two stations are 16 km and 24 km, and the recorded peak ground accelerations (PGAs) are $0.12g$ and $0.09g$, respectively. Figure 12a,b compares the recorded ground motions with the ones simulated by assuming different regional site conditions. Similar to the Northridge event, the simulated acceleration time-history traces and their response spectra agree well with those recorded in the Chi-Chi earthquake by assuming a homogeneous regional site condition ($R_{V_{S30}} = 36$ km). On the other hand, the simulation differs from the recorded time histories if an inappropriate regional site condition ($R_{V_{S30}} = 0$ km) is assumed.

Tables 4 and 5 further compare the PGA, Arias intensity (I_a), and cumulative absolute velocity (CAV, compare with Du and Wang, 2013a) of the recorded and simulated ground motions for both events. Again, it is evident that using a region-specific correlation model yields much better simulation compared with the recorded data, as indicated by the relative errors. On average, the absolute relative error of IMs is less than 10% using the region-specific correlation, whereas the results are scattered and errors are significantly larger if an inconsistent $R_{V_{S30}}$ is used. These results clearly demonstrate the importance of correctly accounting for regional site conditions in the simulation of spatially distributed ground motions.

Conclusions

In this study, a novel technique is developed to simulate regionalized ground-motion time histories using wavelet-packet analysis. Spatial cross-correlation models for four wavelet-packet parameter groups are developed using ground-motion recordings from eight recent earthquakes (Northridge, Chi-Chi, Parkfield, Anza, Alum Rock, Chuetsu, Chino Hills, and El Mayor Cucapah). These wavelet-packet parameters characterize the energy content, time–frequency-domain characteristics, and time–frequency nonstationarity of ground motions. We proposed an LMC to construct a permissible spatial cross-correlation model by using a short-range (5 km) and a long-range (60 km) exponential function.

Analysis of data from eight earthquakes reveals that the spatial cross correlations of wavelet-packet parameters would be stronger if the regional site condition is homogeneous. It is further observed that both of the short-range and long-range coregionalization matrices $\mathbf{P}^1$ and $\mathbf{P}^2$ are dependent on regional site conditions that can be quantified using the correlation range of V_{S30} ($R_{V_{S30}}$). For all four wavelet-parameter groups, the short-range matrix $\mathbf{P}^1$ linearly increases and the long-range matrix $\mathbf{P}^2$ linearly decreases with an increasing $R_{V_{S30}}$ at different rates, showing various degrees of dependence on the regional site conditions. In the end, a set of coregionalization matrices are proposed in Table 3 to quantify the region-specific cross correlations in each group. In addition, a standard deviation matrix is also provided to quantify the goodness of model fitting.

As illustrative examples, blind tests are conducted to evaluate the performance of the spatial cross-correlation model. Ground motions are blindly simulated using neighborhood data from the Northridge and Chi-Chi earthquakes. For each event, two different regional site conditions, one heterogeneous and the other homogeneous, are assumed in the stochastic simulation. The blind test demonstrated that the proper account of regional site conditions can improve the stochastic simulation of regionalized ground motions.

The proposed model is generally applicable to shallow crustal events. Following the same procedure and regression analysis, the model could also be extended to simulate subduction or other types of noncrustal earthquakes if ground-motion databases are available. However, it is also noted that the stochastic model is empirically calibrated based on recorded ground motions using a limited number of parameters. The stochastic model may have difficulty capturing waveform characteristics resulting from complex rupture processes and wave propagation as compared with a physics-based simulation.

Compared with the previous studies on spatial correlation of IMs, the proposed model is among the first of the kind to simulate region-specific spatially correlated waveforms. As demonstrated in the example, the method can interpret

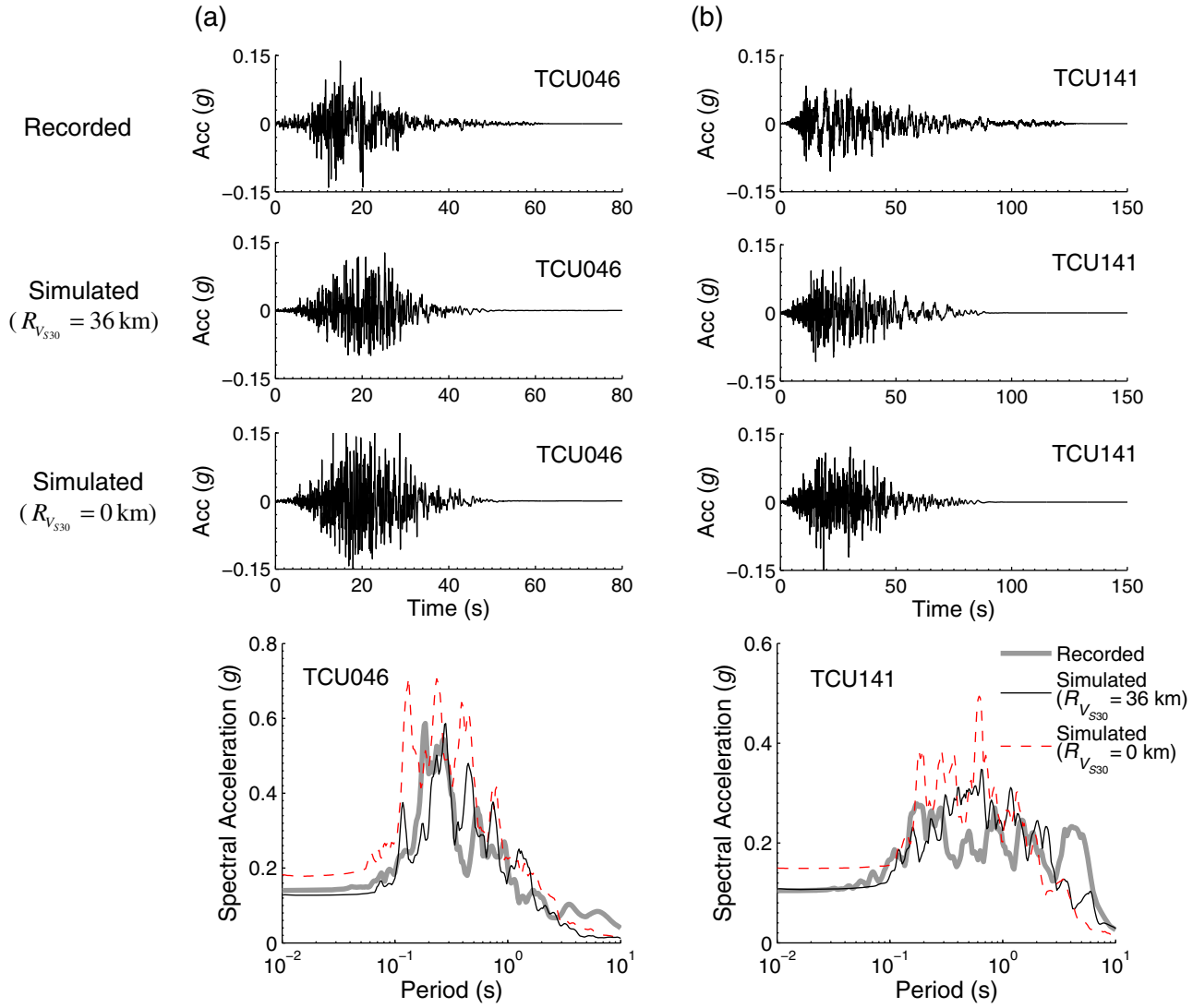

Figure 12. Comparison of recorded and simulated acceleration time histories using different regional site conditions: (a) TCU046 Station (the left column) and (b) TCU141 Station (the right column) for the Chi-Chi earthquake. The color version of this figure is available only in the electronic edition.

Table 4
Recorded and Simulated Ground-Motion Intensity Measures (IMs) Using Different Regional Site Conditions for the Northridge Earthquake

Intensity Measures	Site Condition	Roscoe Boulevard	Relative Error	Baldwin Hills	Relative Error
PGA (g)	Recorded	0.30		0.19	
	$R_{V_{S30}} = 0$ km	0.31	4%	0.18	−5%
	$R_{V_{S30}} = 40$ km	0.21	−29%	0.13	−32%
I_a ($g \times s$)	Recorded	0.14		0.06	
	$R_{V_{S30}} = 0$ km	0.16	11%	0.06	−4%
	$R_{V_{S30}} = 40$ km	0.10	−26%	0.04	−27%
CAV ($g \times s$)	Recorded	1.04		0.78	
	$R_{V_{S30}} = 0$ km	1.11	7%	0.73	−7%
	$R_{V_{S30}} = 40$ km	0.93	−11%	0.63	−19%

Table 5
Recorded and Simulated Ground-Motion IMs using Different Regional Site Conditions for the Chi-Chi Earthquake

Intensity Measures	Site Condition	TCU046	Relative Error	TCU141	Relative Error
PGA (g)	Recorded	0.14		0.10	
	$R_{V_{S30}} = 36$ km	0.13	−9%	0.11	3%
	$R_{V_{S30}} = 0$ km	0.18	28%	0.15	43%
I_a ($g \times s$)	Recorded	0.05		0.07	
	$R_{V_{S30}} = 36$ km	0.06	22%	0.07	4%
	$R_{V_{S30}} = 0$ km	0.11	119%	0.09	20%
CAV ($g \times s$)	Recorded	0.76		1.49	
	$R_{V_{S30}} = 36$ km	0.84	10%	1.38	−7%
	$R_{V_{S30}} = 0$ km	1.17	53%	1.39	−7%

waveforms at unmeasured sites conditioned on recorded wave traces in the neighborhood. The simulated ground motions can enrich the strong-motion database used for ground-motion selection and modification (e.g., Wang, 2011; Wang *et al.*, 2015). More importantly, it has great potential to be used in computationally based seismic-hazard analysis and loss estimation in a regional scale.

Data and Resources

Ground-motion time histories used in this study were retrieved from the Center for Engineering Strong-Motion Data (http://strongmotioncenter.org/; last accessed January 2014), Consortium of Organizations for Strong Motion Observation Systems (http://www.cosmos-eq.org/; last accessed January 2014), K-NET (http://www.kyoshin.bosai.go.jp/; last accessed January 2014), and Pacific Earthquake Engineering Research (PEER) Center's Next Generation Attenuation-West 2 (NGA-West 2) strong-motion database (http://peer.berkeley.edu/ngawest2/databases/; last accessed January 2014). Wavelet-packet simulation of ground motions was modified from the source code at Jack Baker's website (http://www.stanford.edu/~bakerjw/gm_simulation.html; last accessed January 2014).

Acknowledgments

The authors acknowledge financial support from Hong Kong Research Grants Council through Collaborative Research Fund Grant Number CityU8/CRF/13G and Direct Allocation Grant Number DAG08/09.EG01, DAG11EG03G. The authors are also grateful to James Kaklamanos and Christophe Loth for their constructive comments to improve the quality of the paper.

References

Allen, T. I., and D. J. Wald (2009). On the use of high-resolution topographic data as a proxy for seismic site conditions (V_{S30}), *Bull. Seismol. Soc. Am.* **99,** no. 2A, 935–943.

Ancheta, T. D., R. B. Darragh, J. P. Stewart, W. J. Silva, B. S. J. Chiou, K. E. Wooddell, R. W. Graves, A. R. Kottke, D. M. Boore, T. Kishida, and J. L. Donahue (2013). PEER NGA-West 2 database, *PEER Report 2013/03*, 83.

Baker, J. W., and M. K. Miller (2011). Effects of earthquake source geometry and site conditions on spatial correlation of earthquake ground motion hazard, in *Proc. of 4th IASPEI/IAEE International Symposium*, University of California, Santa Barbara, California, 23–26 August.

Chiou, B. S. J., R. Darragh, N. Gregor, and W. Silva (2008). NGA project strong-motion database, *Earthq. Spectra* **24,** 23–44.

Du, W., and G. Wang (2013a). A simple ground-motion prediction model for cumulative absolute velocity and model validation, *Earthq. Eng. Struct. Dynam.* **42,** no. 8, 1189–1202.

Du, W., and G. Wang (2013b). Intra-event spatial correlations for cumulative absolute velocity, Arias intensity, and spectral accelerations based on regional site conditions, *Bull. Seismol. Soc. Am.* **103,** no. 2A, 1117–1129.

Du, W., and G. Wang (2014). Fully probabilistic seismic displacement analysis of spatially distributed slopes using spatially correlated vector intensity measures, *Earthq. Eng. Struct. Dynam.* **43,** no. 5, 661–679.

Esposito, S., and I. Iervolino (2011). PGA and PGV spatial correlation models based on European multievent datasets, *Bull. Seismol. Soc. Am.* **101,** no. 5, 2532–2541.

Goda, K., and H. P. Hong (2008). Spatial correlation of peak ground motions and response spectra, *Bull. Seismol. Soc. Am.* **98,** no. 1, 354–365.

Goovaerts, P. (1997). *Geostatistics for Natural Resources Evaluation*, Oxford University Press, Oxford, New York.

Huang, D., and G. Wang (2014). Stochastic simulation of regionalized ground motions using wavelet packets and cokriging analysis, *Earthq. Eng. Struct. Dynam.*, doi: 10.1002/eqe.2487.

Jayaram, N., and J. W. Baker (2009). Correlation model for spatially distributed ground-motion intensities, *Earthq. Eng. Struct. Dynam.* **38,** 1687–1708.

Jeon, S., and T. D. O'Rourke (2005). Northridge earthquake effects on pipelines and residential buildings, *Bull. Seismol. Soc. Am.* **95,** no. 1, 294–318.

Kaklamanos, J., and L. G. Baise (2011). Model validations and comparisons of the next generation attenuation of ground motions (NGA-West) project, *Bull. Seismol. Soc. Am.* **101,** no. 1, 160–175.

Loth, C., and J. W. Baker (2013). A spatial cross-correlation model of ground motion spectral accelerations at multiple periods, *Earthq. Eng. Struct. Dynam.* **42,** 397–417.

O'Rourke, T. D., and S. S. Jeon (2002). GIS loss estimation and post-earthquake assessment of residential building damage, in *Proc. of the 7th National Conference on Earthquake Engineering*, Boston, Massachusetts, 21–25 July, EERI, Oakland, California.

Sokolov, V., and F. Wenzel (2011). Influence of spatial correlation of strong ground motion on uncertainty in earthquake loss estimation, *Earthq. Eng. Struct. Dynam.* **40,** 993–1009.

Sokolov, V., and F. Wenzel (2013). Further analysis of the influence of site conditions and earthquake magnitude on ground–motion within–earthquake correlation: Analysis of PGA and PGV data from the K-NET and the KiK-net (Japan) networks, *Bull. Earthq. Eng.* **11,** 1909–1926.

Sokolov, V., F. Wenzel, K.-L. Wen, and W.-Y. Jean (2012). On the influence of site conditions and earthquake magnitude on ground-motion within-earthquake correlation: Analysis of PGA data from TSMIP (Taiwan) network, *Bull. Earthq. Eng.* **10,** 1401–1429.

Wang, G. (2011). A ground motion selection and modification method capturing response spectrum characteristics and variability of scenario earthquakes, *Soil Dynam. Earthq. Eng.* **31,** 611–625.

Wang, G., and W. Du (2013). Spatial cross-correlation models for vector intensity measures (PGA, I_a, PGV and SAs) considering regional site conditions, *Bull. Seismol. Soc. Am.* **103,** no. 6, 3189–3204.

Wang, G., R. Youngs, M. Power, and Z. Li (2015). Design ground motion library (DGML): An interactive tool for selecting earthquake ground motions, *Earthq. Spectra* **31,** no. 1, doi: 10.1193/090612EQS283M.

Yamamoto, Y. (2011). Stochastic model for earthquake ground motion using wavelet packets, *Ph.D. Thesis*, Department of Civil and Environmental Engineering, Stanford University, Stanford, California, 60.

Yamamoto, Y., and J. W. Baker (2013). Stochastic model for earthquake ground motion using wavelet packets, *Bull. Seismol. Soc. Am.* **103,** no. 6, 3044–3056.

Department of Civil and Environmental Engineering
Hong Kong University of Science and Technology
Clear Water Bay, Kowloon
Hong Kong SAR, China
drhuang@ust.hk
gwang@ust.hk

Manuscript received 6 July 2014;
Published Online 13 January 2015